JOURNAL OF PROPULSION AND POWER
Vol. 26, No. 5, September–October 2010

# Numerical Investigation of the Supersonic Combustion of Kerosene in a Strut-Based Combustor

K. Kumaran,* Prabhat Ranjan Behera,† and V. Babu‡
*Indian Institute of Technology, Madras 600 036, India*

DOI: 10.2514/1.46965

**In this numerical study, supersonic combustion of liquid kerosene in a strut-based combustor is investigated. To this end, three-dimensional compressible, turbulent, nonreacting and reacting flow calculations with a single-step chemistry model have been carried out. For the nonreacting flow calculations, fuel droplet trajectories, degree of mixing, and mixing efficiency are presented and discussed. For the reacting flow calculations, contours of heat release and Mach number and the variation of combustion efficiency, total pressure loss, and thrust profile along the combustor length are used to identify the regions of mixing and heat release inside the combustor. Furthermore, the predicted variation of static pressure along the combustor top wall is compared with experimental data. The significance of the lateral spread of the fuel and the extent of the mixing process, especially for a liquid fuel such as kerosene, on the prediction of heat release is discussed in detail.**

## I. Introduction

AIRBREATHING engines are considered to be the most appropriate alternative propulsion device to rocket-based space vehicles within the atmospheric limit. Supersonic combustion ramjet (scramjet) engine is the key enabling technology for such sustained hypersonic flights. In scramjet engines, the combustor length is typically of the order of 1 m, and the residence time of the fuel–air mixture is of the order of a millisecond (for flight Mach numbers from 6 to 8). Generation of useful thrust over the vehicle drag through heat addition at such high speeds is challenging, owing to the fact that the fuel has to mix and burn completely within the short combustor length. In addition, in the lower hypersonic regimes ($M < 8$) that are of current interest, a liquid hydrocarbon fuel, such as kerosene, is desirable, owing to its high volumetric energy content and relative ease of handling. However, the liquid fuel has to atomize and evaporate before mixing with the mainstream air. This adds an additional time delay to the heat release, necessitating a longer residence time and, in turn, a longer combustor length. All these issues clearly highlight the fact that mixing plays a crucial role in supersonic combustion.

Research, both experimental and numerical, on supersonic mixing and combustion is being carried out around the world for the development of a scramjet engine. Several fuel-injection strategies, such as strut [1,2], wall [3,4], and ramp [5], and integrated flame holding/fuel-injection strategies, such as cavity configurations [6], have been investigated in full-scale combustors in the recent past. Numerical investigations [2,5] have shown that, with staged fuel-injection schemes, full-scale combustors can accommodate a larger heat release with a higher equivalence ratio without altering the inlet conditions. Further, in full-scale combustors, detailed chemistry was shown to be important only in the mixing controlled regions, while the thin flame model was reported to be adequate for the prediction of the diffusion flame zone [2,3]. For flight Mach numbers ranging from $M = 4$ to 8, the scramjet engine was shown to operate in a dual-mode condition [3,6].

Received 1 September 2009; revision received 19 March 2010; accepted for publication 23 March 2010. 

*Ph.D. Scholar, Department of Mechanical Engineering.
†M.Tech. Student, Department of Mechanical Engineering,
‡Professor, Department of Mechanical Engineering; vbabu@iitm.ac.in (Corresponding Author).

With the exception of the works cited previously, the majority of the results available in the literature on supersonic combustion are on model combustors. The successful development of a scramjet engine depends on extending the findings from model combustors to full-scale combustors. Ground testing of a full-scale combustor demands a high-enthalpy wind tunnel with an ejector facility, which is difficult to develop. In view of this constraint, and with the advancement in computational resources, computational fluid dynamics (CFD) can play a major role in assessing and improving the preliminary designs. Recently, Rajasekaran and Babu [5] presented the outcome of such an effort. Here, numerical predictions of a concept supersonic combustor using kerosene fuel were presented. However, there was no validation of the predictions with experimental data. In the present study, the supersonic combustion of kerosene is numerically investigated in a strut-based, staged injection full-scale supersonic combustor, and the wall static pressure predictions are validated with experimental data. All the calculations have been performed using FLUENT [7].

## II. Computational Methodology

The schematic of the combustor geometry investigated is shown in Fig. 1. The combustor has four segments. Segment I is a constant area isolator segment located between the combustor and the intake segment. This is followed by three diverging segments (labeled as II, III, and IV in Fig. 1) of varying lengths and divergence angles. The full-scale combustor has a total of five struts grouped in three stages. The spanwise staggered arrangement of the struts is intended to achieve uniform fuel injection and distribution across the entire cross section, with minimal blockage. The axial location of the struts is expected to result in the heat release occurring toward the end of segment II and in segment III. In addition, heat release from the combustion of the fuel injected from the first-stage strut is expected to act as an ignition source for the fuel injected from second- and third-stage struts. The divergence that is provided on the upper wall is designed to avoid thermal choking for the operating condition studied here. Based on symmetry consideration, all the computations have been carried out in one-half of the combustor geometry, shown in Fig. 1.

Kerosene is injected from the struts in the direction normal to the strut surface (i.e., in the positive and negative $z$ direction). A close-up view of the strut is shown in Fig. 2. The row of dots on the strut surface in this figure indicates the fuel-injection locations. Each strut has a total of 22 injectors (11 injectors on either side of the strut), each with a diameter of 0.6 mm. In each strut, V gutters are also provided for flame stabilization and to enhance mixing. The number of V gutters on the struts is different for different stages. In all the struts,

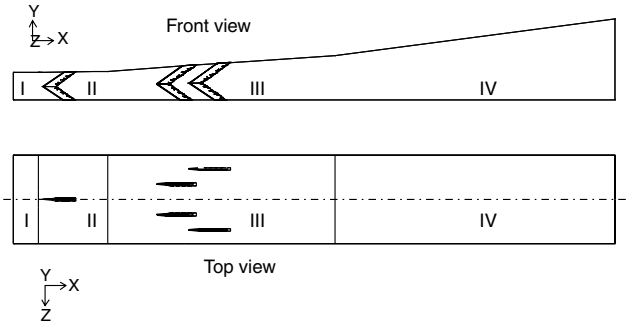


**Fig. 1 Schematic of the full-scale supersonic combustor. Flow is from left to right.**

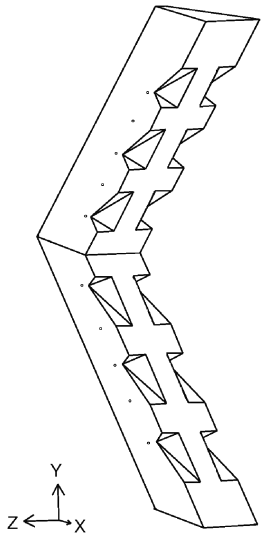


**Fig. 2 A close-up view of the strut rear side.**

the fuel injectors are located upstream of the V gutters in order to increase the residence time and, in turn, the mixing.

In an earlier investigation [8], the fuel injectors were modeled as surface injectors, wherein droplets were injected from each discretized face of the injector with a uniform diameter. Since the injector dimension is usually very small when compared with the dimensions of the combustor, very fine meshing is necessary to have at least a few facets on the injection surface. Meshing the volume containing the injector face and blending it smoothly (i.e., with acceptable skewness of the cells) with the mesh in the surrounding volumes is usually a formidable task. Although it is possible to prescribe a distribution for the droplet diameter in the surface injection model, it is somewhat unrealistic to do so when the number of streams is very small. Hence, a constant droplet diameter was used in the earlier work [8]. This shortcoming was identified to result in excessive heat release locally and, thus, unreasonably high temperatures [8]. Later, in the same model combustor configuration, the fuel injection was modeled as a spray [9], using the available details on the injection parameters as well as the visualization of the spray [10]. With the spray model, the effect of injection pressure on the droplet diameter and penetration could be investigated. The numerical simulations were able to predict the mixing and combustion characteristics in the model combustor well, and the predicted wall static pressure distribution was close to the experimental values reported by Yu et al. [11]. The same approach was attempted with the present full-scale combustor but had to be abandoned due to the lack of details on the spray injected into the supersonic crossflow. Consequently, here, the fuel injection is modeled as surface injection, with the droplet diameters obeying a Rosin–Rammler distribution after ensuring that the number of fuel streams from each injector is sufficiently large.

In the present work, each injector surface is meshed in such a way that the injector surface is discretized into 12 facets. On each injector surface, the number of diameter sets are specified to be five. This will result in 60 fuel streams from each injector. The droplet diameters obey a Rosin–Rammler distribution with the minimum, maximum, and mean droplet diameter being 5, 50, and 33 $\mu$m, respectively, and the spread parameter is taken to be 3.9. The Sauter mean diameter [12] comes out to be 35 $\mu$m. These values are chosen by extrapolating the inferences drawn from an earlier study [9], where the effect of injection pressure on the droplet diameter distribution was investigated. These values are expected to represent the actual conditions to a reasonable extent. Sensitivity of the prediction to these values, however, has not been attempted.

In the simulations, three-dimensional, compressible, and turbulent Favre-averaged Navier–Stokes equations are solved along with the species conservation equation for the continuous phase. The calculations have been carried out using the one-equation Spalart–Allmaras model [13]. Default values have been used for the model constants ($C_{b1} = 0.1355$, $C_{b2} = 0.622$, $C_{v1} = 7.1$, $C_{w2} = 0.3$ $C_{w3} = 2.0$, and $\kappa = 0.4187$). This model has been successfully used for modeling supersonic combustion of kerosene in model combustors [9]. The turbulent Schmidt number and Prandtl number are taken to be equal to 0.7 and 0.667, respectively. Sensitivity of the numerical predictions to the turbulent Schmidt number for ethylene [6] and hydrogen [14] fuels has been investigated already.

Since kerosene is injected in liquid phase in the form of droplets, the simulations have been performed using a discrete phase model. Here, in addition to solving the transport equations for the continuous phase, the discrete phase (dispersed in the continuous phase) is simulated in a Lagrangian frame of reference. Mass, momentum, and energy transfer between the two phases is accounted for in the simulations. The drag force on the dispersed droplets is calculated using the high Mach-number law [15]. Dispersion of the droplets due to turbulence has been ignored in the calculations, as it is not possible to model this effect in conjunction with a one-equation turbulence model for the continuous phase. Droplet breakup also has been ignored. This will likely result in an underprediction of the heat release, whereas neglecting the dispersion will underpredict the overall mixing and the combustion efficiency [9].

Single-step laminar finite-rate kinetics has been used to model the chemistry. Rate data for the $C_{12}H_{23} - O_2$ forward reaction mechanism has been adapted from Westbrook and Dryer [16]. Viscosity and $C_p$ of the mixture have been evaluated using a mass-weighted-mixing law. For the individual fluids in the mixture, these properties have been evaluated using Sutherland's law and fifth-order polynomials in temperature, respectively.

### A. Boundary Conditions

At the combustor inlet (where the flow is supersonic), stagnation and static pressure, stagnation temperature, and species mass fractions are specified. Vitiated air (with the mass fractions of $O_2$, $H_2O$, $CO_2$, and $N_2$ being 0.123, 0.188, 0.00034, and 0.6886, respectively) enters the combustor at a nominal Mach number of two.[§] In addition, inlet turbulence intensity (10%) and the hydraulic diameter (to estimate the turbulent length scale) have been specified. All the flow variables at the combustor outlet, including pressure, are determined from the interior of the domain by extrapolation, since the flow is supersonic here. All the walls are considered stationary and adiabatic, and standard wall functions have been used. For the discrete phase, injection parameters, namely, the mass flow rate of kerosene (corresponding to an equivalence ratio of one), temperature, and velocity are specified.

### B. Grid Refinement Study

The computational domain is meshed with a hybrid mesh (involving hexahedral and tetrahedral cells). To facilitate the hybrid meshing, the computational domain is divided into 14 smaller

[§]These values represent the actual inlet conditions during ground testing of the full-scale combustor.

volumes. The volumes enclosing the struts are meshed with tetrahedral cells, owing to the geometric complexity of the struts. However, effort has been taken to ensure that the skewness of the tetrahedral cells is acceptable. Here, the volume-weighted equiangle skew of the tetrahedral mesh is 0.35. The final mesh consists of 886,187 hexahedral cells and 1,024,686 tetrahedral cells. Although the volume occupied by the tetrahedral cells is much less than the volume occupied by the hexahedral cells, their number is higher, owing to the necessity to resolve the intricate geometric details (such as the injection port) and blend with the outlying hexahedral mesh with an acceptable degree of skewness.

For a computational domain such as the present one, grid refinement (adaptation) based on the gradients of the flow variables in the solver will drastically increase the cell count, and it would be computationally too expensive. Hence, the grid has been remeshed outside the solver, based on the results obtained using the existing mesh. The remeshing is done until flow features, such as shocks and expansion fans, do not change with further refinement. Also, in the regions of heat release, the mesh has been refined (i.e., remeshed) until there were no significant changes in the solution. After all these refinements, a grid with a cell count of 1,910,873 has been taken as the final grid. All the cold flow and the reacting flow calculations have been carried out on this mesh. The details of the maximum and the area-weighted values of wall $y^+$ for the cold flow (without and with fuel injection) and reacting flow calculations in this mesh are given in Table 1. Except for some isolated spots in the vicinity of the injection ports, wall $y^+$ is generally between 40 and 100.

### C. Convergence Metrics

The accuracy of the solutions have been assessed through additional metrics, such as global mass, momentum, and energy balance. For all the results reported here, the difference in the mass flow rate between the inlet(s) and outlet is less than 1% of the injected fuel mass flow rate (fuel mass flow rate rather than the inlet mass flow rate is used, since the former is less than the latter by an order of magnitude). The integrated value of the fuel mass flow rate for the nonreacting and reacting flow at various $x =$ constant planes downstream of the injection locations is within 5% of the injected fuel mass flow rate. This serves as a check on global fuel conservation. Momentum balance has been checked by evaluating the left- and right-hand sides of the expression

$$\mathcal{F} = \left( \int p \, \mathrm{d}A + \int \rho u^2 \, \mathrm{d}A \right)_{\text{inlet}}^{\text{exit}}$$

separately and then calculating the difference. The right-hand side of this expression is the impulse function. The left-hand side is the net force acting on the walls (pressure and viscous) in the $x$ direction. For all the results reported here, the difference between the left- and right-hand sides of the above expression (for the continuous phase) is less than 5%. The overall energy balance is satisfied to within 5% of the inlet total enthalpy. All the calculations are second-order accurate.

## III. Results and Discussion

In this section, results from the nonreacting and reacting flow calculations are presented and discussed. The combustion efficiency, total pressure loss, thrust profile along the combustor length, and the comparison of wall static pressure (along the combustor top wall) with the experimental values are also discussed.

### A. Nonreacting Flow

Figure 3 shows a schlieren picture of the flowfield. The curved bow shock ahead of the struts and the oblique shocks from the trailing-edge corners of the struts can clearly be seen on the top wall. Since the struts are V shaped, the shock structures are three-dimensional, as the footprint of these shocks on the combustor sidewall show. Reflection of these shocks from the symmetry plane, as well as the sidewall, are also clearly visible. The expansion fan on the top wall, owing to the change in the slope from one segment of the combustor to another, can also be seen. The flow accelerates continuously in the diverging segment and reaches an area-averaged Mach number of 2.48 at the combustor exit.

In segment III (where the second- and third-stage struts are present), the interaction of the shocks and the expansion fans and their complex nature are clearly seen on the top wall in Fig. 3. In the injection case, fuel is injected in the $z$ direction from the injectors located on the strut side faces. This results in an additional pressure rise, due to the shocks generated ahead of the fuel jet as it is injected into the supersonic mainstream air.

Figure 4 shows the close-up view of the fuel droplet trajectories and the gradient of the liquid phase density on a $y =$ constant plane passing through the injector located midway along the strut. Trajectories of the droplets released from the last strut alone are shown for the sake of clarity. The schlieren picture shows the penetration and spreading of the kerosene spray clearly. The staggered arrangement of the struts and the injection of fuel normal to the flow direction result in an expanding fan of fuel droplets starting from the first strut, which eventually fills the entire cross section. It is clear from Fig. 4 that the fuel trapped behind the strut (i.e., in the wake region) evaporates completely. This will result in a high concentration of kerosene vapor in the wake region behind the struts. Consequently, the heat release is likely to start in the wake region and then spread across the cross section. In addition, this arrangement is also expected to result in an uniform heat release across the combustor cross section. A few of the fuel streams injected from the third-stage strut are seen to impinge on the sidewalls. This may result in excessive heat release near the sidewall, leading to a continuous exposure to high temperature and thermal stress on the sidewalls.

Figure 5 shows contours of the kerosene vapor mass fraction on $x =$ constant planes at different axial locations. The $x =$ constant planes are labeled alphabetically to facilitate the discussion. The fuel injected from the first-stage strut vaporizes and moves toward the low-velocity region behind the strut, as seen in plane A. Further downstream, the kerosene vapor spreads out (as seen in plane B). In addition to this, the fuel injected from the second- and third-stage struts considerably increases the kerosene mass fraction in the middle of the combustor (as seen in planes D and E). Downstream of plane E, the fuel mass fraction is higher in the middle of the combustor and spreads out toward the combustor walls. This, in turn, indicates that the heat release is likely to start from the middle of the combustor and spread outward. However, the fuel is not seen to spread completely near the sidewall until the combustor exit. This can be due to the fact that the fuel streams injected from the strut close to the sidewall are pushed toward the core region by the mainstream flow. This can be seen in Fig. 4 (top). The fuel mass concentration in the region between the second and third struts is high; hence, the heat release in the low-velocity region downstream of first strut may play a significant role in igniting the additional fuel injected downstream. Figure 5 gives a qualitative measure of the fuel spread across the combustor cross section. Since the primary objective of the staggered arrangement of the struts is to increase the fuel spread, and in turn the heat release across the combustor, a quantitative evaluation is

**Table 1 Grid refinement study for nonreacting and reacting flow calculations**

| Model | No. of cells | Maximum wall $y^+$ | Average wall $y^+$ |
|---|---|---|---|
| Cold flow (without injection) | 1,910,873 | 220 | 103 |
| Cold flow (with injection) | 1,910,873 | 220 | 111 |
| Reacting flow | 1,910,873 | 220 | 90 |

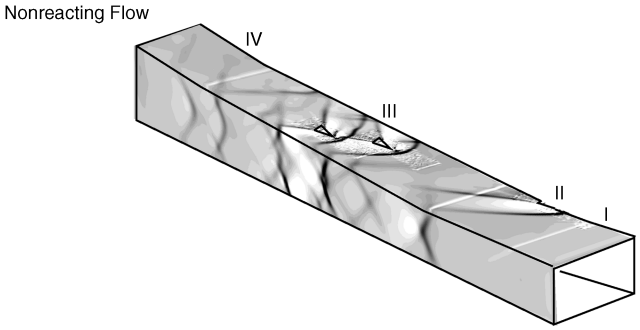


**Fig. 3 Schlieren image on the combustor top and sidewalls for the cold flow calculations without fuel injection.**

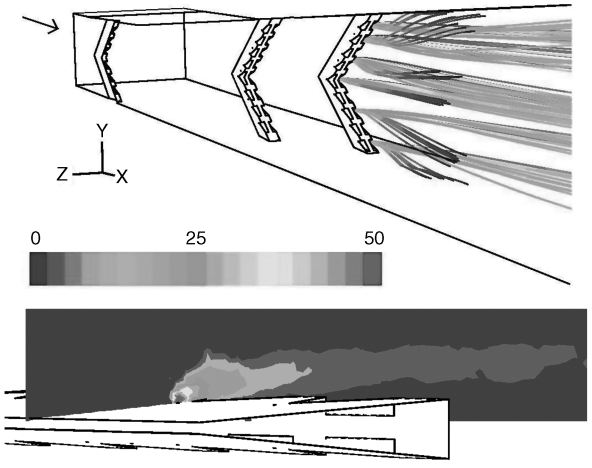


**Fig. 4 Fuel droplet trajectories colored with droplet diameter (in microns) (top) and the schlieren image of the kerosene spray from one of the injectors, viewed from above (bottom).**

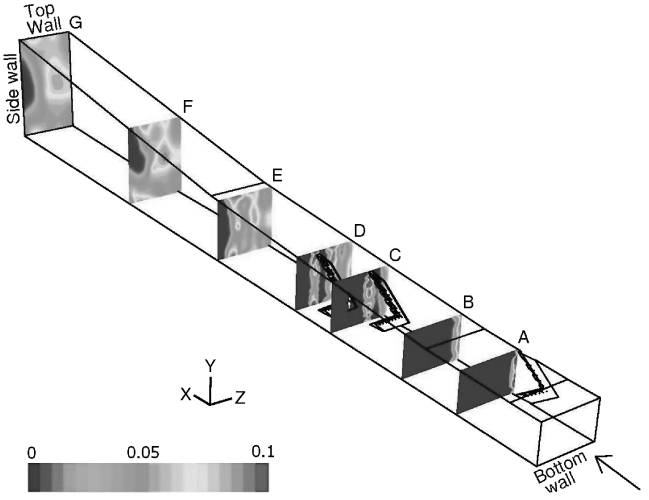


**Fig. 5 Contours of kerosene vapor mass fraction at different axial locations for the entire combustor.**

necessary to help the designer in optimizing the fuel-injection strategy. This is discussed next.

The degree of mixing is calculated to quantify the spatial distribution of the fuel across the combustor cross section. Here, the degree of mixing $D_m$ on an $x =$ constant plane is calculated as follows:

$$D_m = \frac{\int_x \phi \, \mathrm{d}A}{A_x}; \qquad \phi = \begin{cases} 1, & \alpha > \alpha_{\min} \\ 0, & \alpha < \alpha_{\min} \end{cases}$$

where $\alpha$ is the fuel mass fraction, $\alpha_{\min}$ is a cutoff value for the mass fraction of kerosene vapor on that plane, and $A_x$ is the cross-sectional area of the combustor at this axial location; $\alpha_{\min}$ is taken to be equal to 10% of the maximum value of the kerosene vapor mass fraction on that plane. The cutoff value chosen here serves to clearly demarcate the boundary of the fuel spread in each plane. This is customarily done in experiments for determining the penetration height of the fuel stream.

Figure 6 shows the axial variation of the degree of mixing from downstream of the first strut until the combustor exit. The struts are also indicated in this figure to facilitate the discussion. The fuel injected from the first-stage strut shows a gradual lateral spread. Further downstream, with additional fuel injected from the second- and third-stage struts, the spread increases monotonically in segment III. This can be due to two reasons: 1) the staggered arrangement of the second- and third-stage struts, and 2) the diffusion time scale may be less when compared with the flow time scale, since the main flow has been decelerated across the shocks in this region. In the latter case, in addition to a better spread, the fuel can also be expected to mix locally with the main flow at a stoichiometric ratio. This can be ascertained with the help of mixing efficiency, which is discussed later. Beyond $x/L = 0.4$, the lateral spread of the fuel is gradual. This can be attributed to the fact that the flow time scale may be comparable with the diffusion time scale, owing to the expansion and acceleration of the flow in the diverging segment. The degree of mixing reaches a maximum value of 94% at the combustor exit. This clearly brings out the fact that, with the staggered arrangement of the struts and, in turn, the fuel-injection system, a very high lateral spread can be achieved, even for a liquid fuel such as kerosene, where the liquid has to atomize and evaporate before mixing.

The degree of mixing discussed previously quantifies the physical spreading of the fuel across the combustor cross section. For combustion, stoichiometry is more important than the mere presence of fuel. In the present work, this is evaluated using a mixing efficiency [17], which is defined as follows:

$$\eta_m = \frac{\int_x \alpha_R \rho u \, \mathrm{d}A}{\sum_x \dot{m}_{\text{fuel,in}}}; \qquad \alpha_R = \begin{cases} \alpha & \alpha \le \alpha_s \\ \alpha_s \frac{1-\alpha}{1-\alpha_s} & \alpha > \alpha_s \end{cases}$$

where $\alpha$ is the actual fuel mass fraction, $\alpha_s$ is the stoichiometric fuel mass fraction corresponding to the oxygen mass fraction at that location, $\rho$ is the density, $u$ is the axial velocity, and $\dot{m}_{\text{fuel,in}}$ is the mass flow rate of fuel injected upstream of this plane. The denominator represents the total amount of fuel injected upstream of that plane. Mixing efficiency is thus a measure of the percentage of the fuel that is likely to burn under stoichiometric conditions.

The variation of the mixing efficiency along the combustor length is shown in Fig. 7. It can be seen that the fuel injected from the first strut mixes rapidly from $0.15 \le x/L \le 0.2$. In the region $0.2 \le x/L \le 0.35$, the mixing efficiency decreases, due to more

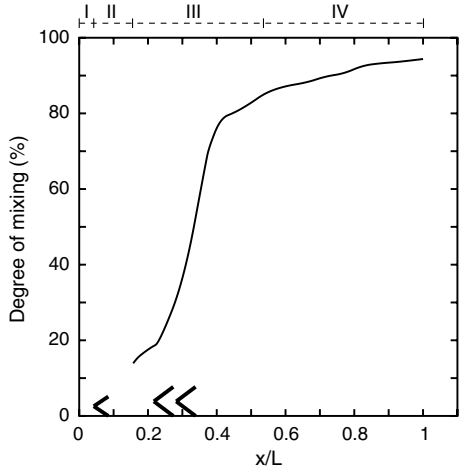


**Fig. 6 Variation of the degree of mixing along the combustor length.**

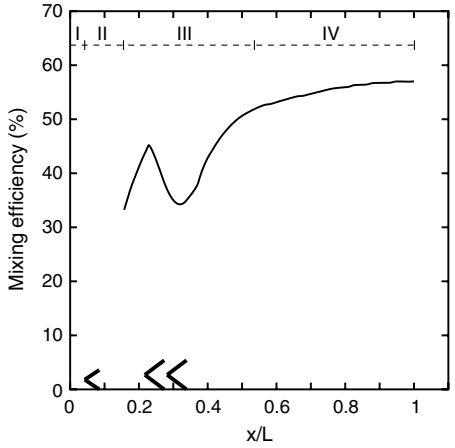


**Fig. 7 Variation of mixing efficiency along the combustor length.**

fuel being injected from the second and the third row of struts. Further downstream, the mixing efficiency increases steeply up to $x/L = 0.5$; thereafter, the increase is gradual and reaches a maximum of 57% at the combustor exit. In segment III, although the degree of mixing reaches a value higher than 80%, the mixing efficiency is only about 50%. This, in turn, indicates that, although the fuel has spread across 80% of the combustor cross section, only 50% of the injected fuel has mixed at stoichiometric proportion (i.e., likely to undergo complete combustion). Further, the mixing levels off by $x/L = 0.6$, or about 60% of the combustor length. At the combustor exit, about 4.4% of the injected fuel leaves in liquid form and the remaining in vapor form.

### B. Reacting Flow

Figure 8 shows the contours of heat release on $x =$ constant planes at different axial locations. Since any increase in stagnation temperature has to be solely due to heat release from combustion, the dimensionless heat release at a location is calculated as $T_0/T_{0,\text{inlet}} - 1$. In planes A and B, the negative value for the heat release indicates the mixing of the low-temperature fuel stream, with the mainstream at a higher stagnation temperature. As speculated earlier, the heat release starts from the low-velocity region downstream of the strut in segment II, as seen in plane B. In plane C, the heat release spreads out toward the symmetry plane. Further downstream, in planes D and E, the heat release spreads toward the sidewall. The heat release contours in planes D to G in Fig. 8 are similar to the contours of fuel mass fractions on these planes in Fig. 5. The regions of lesser heat release in these planes coincide well with regions of lower fuel mass fractions in Fig. 5. The staged injection strategy used here helps to achieve a good amount of heat release without altering the combustor inlet condition, and the staggered arrangement helps in achieving a better spread of heat release across the cross section. The contours of the combustion product $CO_2$ on all these planes are similar to the heat release contours; hence, they are not shown.

Figure 9 shows the contours of Mach number on $x =$ constant planes at different axial locations for the reacting flow case. In plane A, the flow is completely supersonic and there is no inlet interaction as a result of the heat release. It can be seen by comparing Figs. 8 and 9 that, in planes A and B, the heat release essentially takes place in the low-velocity wake region behind the first strut. In plane C, the flow separates from the sidewalls near the top and bottom corners and in a few regions near the second strut, due to the pressure rise that accompanies the heat addition. In segment III, comparison of these contours with the contours of heat release shows that, in the regions of heat release downstream of the second- and third-stage struts, the flow is still supersonic. This is interesting, since a staged combustor operating with an equivalence ratio of one may be reasonably expected to operate in a dual mode. The divergence of the top wall allows the flow to expand and accelerate, which helps in maintaining the flow at a supersonic Mach number. Further downstream [i.e, beyond the third strut (planes D to G)], due to the expansion and the diminishing heat release, the flow becomes supersonic across the entire combustor cross section. The area-averaged Mach number at the combustor exit is 1.88, which is considerably less when compared with the cold flow, as a result of the heat addition.

Combustion efficiency is one of the key performance metrics used to evaluate a combustor. Here, the combustion efficiency is calculated based on the fuel consumption at any given $x =$ constant plane. Hence, it gives an indication of the completeness of the combustion process at a given location. Combustion efficiency on a given $x =$ constant plane is given as [17]

$$\eta_c = \frac{\int_x (167/12 \times 44)\alpha \rho u \, \mathrm{d}A}{\sum_x \dot{m}_{\text{fuel,in}}}$$

where $\alpha$ is the mass fraction of $CO_2$, and the multiplicative constant in the numerator accounts for the fact that 12 kmole ($12 \times 44$ kg) of $CO_2$ are produced from the combustion of 1 kmole (167 kg) of fuel.

Figure 10 shows the variation of combustion efficiency along the combustor length. In the region up to $x/L = 0.25$, the combustion efficiency increases continuously due to the heat release from the fuel injected from the first strut. In segment III, the combustion efficiency shows a monotonic increase in contrast to the mixing efficiency. This is due to the fact that additional fuel is injected in segment III; hence, the amount of heat released is also higher in this region. Similar to the

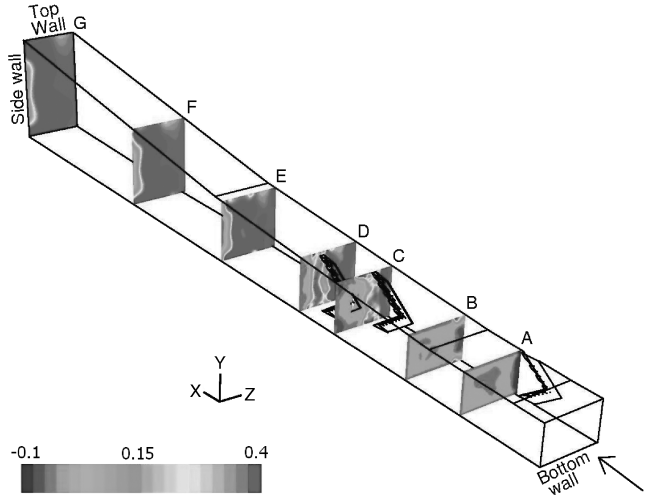


**Fig. 8 Contours of dimensionless heat release at different axial locations along the combustor length.**

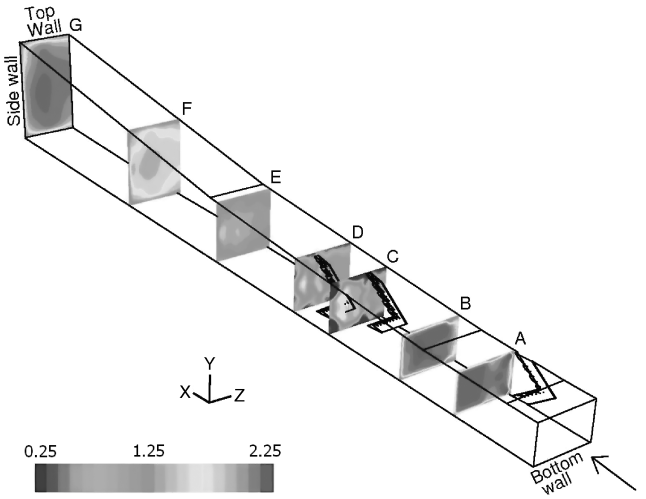


**Fig. 9 Contours of Mach number at different axial locations along the combustor length.**

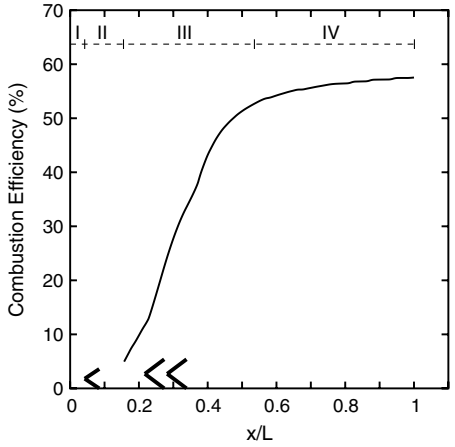


**Fig. 10 Variation of combustion efficiency along the combustor length.**

mixing efficiency, the heat release also levels off beyond $x/L = 0.5$, and the maximum value at the combustor exit is close to the maximum value for the mixing efficiency. The calculations predict that 41.2% of the injected fuel leaves the combustor unburnt, out of which 1% is in liquid form and the rest in vapor form. This clearly highlights the fact that there is room for improvement in the combustion efficiency and, in turn, the useful thrust. With improvements in the combustion efficiency, the overall thrust can be increased, keeping the amount of fuel the same, or the same amount of thrust can be generated with a lesser quantity of fuel.

Figure 11 shows the variation of the total pressure loss ($\eta_t$) for the nonreacting flow (without and with fuel injection) and the reacting flow calculations. This delineates the total pressure loss due to mixing and heat release. Here, the loss in stagnation pressure is calculated as $\eta_t = 1 - (P_{0x}/P_{0,\text{inlet}})$, where $P_{0x}$ is the area-averaged stagnation pressure at any $x =$ constant plane, and $P_{0,\text{inlet}}$ is the stagnation pressure at the combustor inlet. Upstream of the first strut, the total pressure loss is very minimal and is the same for all the cases. Hence, the $\eta_t$ is shown only from $x/L = 0.15$ in all the cases. In the nonreacting flow (without fuel injection), the total pressure loss increases due to the shocks generated from the first strut. In the region $0.25 \leq x/L \leq 0.4$, the total pressure loss increases steeply due to the presence of multiple shocks from the second and third row of struts and the interaction between them, as seen in the top wall in Fig. 3. Beyond $x/L = 0.4$, the increase in total pressure loss is gradual until the combustor exit.

Any difference in total pressure loss between the cold flow (without fuel injection) and the mixing case (cold flow with fuel injection) will essentially be due to the thermodynamic irreversibility of the mixing of the fuel and air. The higher the extent of mixing, the higher the loss in stagnation pressure due to the increase in entropy. The loss of stagnation pressure can thus be used to assess the degree and extent of mixing. Hence, in addition to the cold flow, the variation of the loss in total pressure for the mixing case (cold flow with fuel injection) is also shown in Fig. 11. The variation of the total pressure loss corroborates well with the mixing efficiency curve shown in Fig. 7. In the initial region, although there is a considerable increase in the mixing efficiency, the loss in total pressure due to mixing is not very high, since the fuel injected thus far is only a fraction of the total amount. However, at $x/L = 0.4$, the total pressure loss is high in the mixing case, owing to the addition of more fuel from the second- and third-stage struts. Beyond $x/L = 0.5$, the increase in the mixing efficiency and the total pressure loss is gradual. This indicates that the mixing time scale (across the combustor cross section) is longer, owing to the acceleration of the flow in the diverging segment. This corroborates well with the trends in the degree of mixing in Fig. 6.

Similarly, any difference in the total pressure loss between the mixing and the reacting flow calculations has to be due to increase in entropy from the heat release. A considerable amount of heat release takes place in the region between the first- and the second-stage struts and, consequently, the loss in total pressure is also higher for the reacting flow case. In the region $0.25 \leq x/L \leq 0.4$, there is a steep increase in the total pressure loss in the reacting flow case, owing to higher heat release from the fuel injected from the second- and third-stage struts. At $x/L \approx 0.35$, where the third-stage strut ends, it is clear from Fig. 11 that the loss in total pressure due to heat release from the additional fuel is much higher when compared with the loss due to mixing of the additional fuel. This corroborates well with the combustion efficiency discussed earlier. Beyond $x/L \approx 0.35$, the difference in $\eta_t$ between the mixing and the reacting flow case is almost the same until the combustor exit. This can be attributed to the diminishing of the heat release in the diverging segment, where the flow expands and accelerates. This also correlates well with the trend exhibited by the combustion efficiency. Thus, in addition to the mixing and combustion efficiencies, the total pressure loss is also useful in quantifying the extent of the mixing and the amount of heat release inside the combustor.

Figure 12 shows the thrust profile along the combustor length. Here, the thrust percentage is defined as the ratio of the difference in the impulse function between any $x =$ constant plane and the inlet to that between the outlet and the inlet. The location of the different stages of struts are shown along with the thrust variation. It is clearly seen from Fig. 12 that, despite the heat release downstream of the first strut, the thrust profile shows a decreasing trend. This highlights the fact that the thrust generated in this region is less when compared with the form and pressure drag in this part of the combustor. Further downstream, the additional heat release from the combustion of the fuel injected from the second strut generates a positive thrust. Thus, the thrust profile shows an increasing trend in the region $0.175 \leq x/L \leq 0.3$. Useful thrust generation starts only downstream of the second-stage strut (i.e, $x/L > 0.3$). Thereafter, the

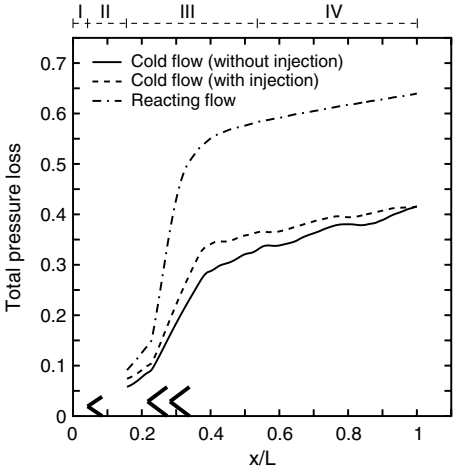


**Fig. 11 Variation of the total pressure loss along the combustor length.**

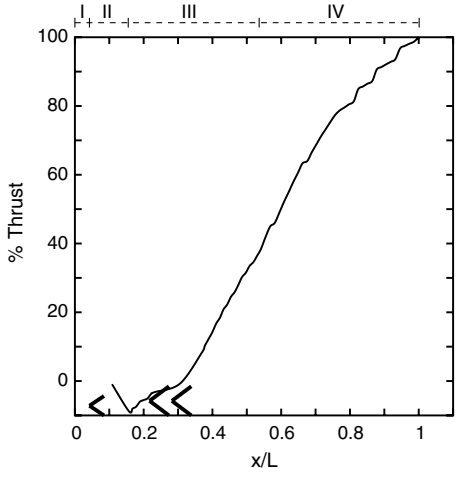


**Fig. 12 Variation of the thrust percentage along the combustor length.**

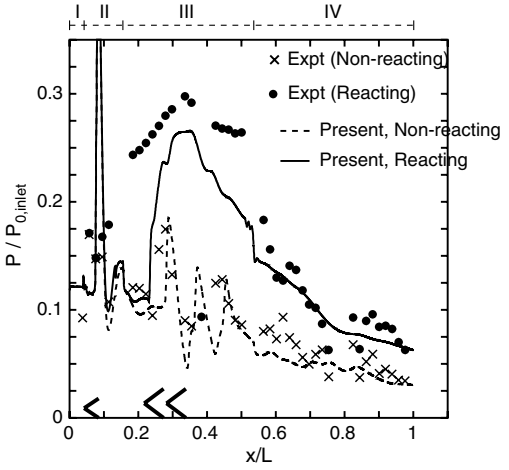


**Fig. 13 Variation of the static pressure on the combustor top wall for the nonreacting (without injection) and reacting flow cases.**

thrust increases continuously until the combustor exit. The uniform thrust profile in segments III and IV attests to the continuous heat release and expansion in these parts of the combustor.

All the results discussed previously clearly demonstrate the extent of the lateral spread of the fuel, mixing, and heat release, and, in turn, the thrust generation for the designed full-scale supersonic combustor.

### C. Comparison with Experimental Data

Figure 13 shows the comparison of the predicted static pressure on the combustor top wall for the nonreacting flow (without fuel injection) and reacting flow with the experimental data. The wall static pressure data along the entire combustor length is taken from the symmetry plane side. In both cases, the sharp increase in pressure at $x/L = 0.1$ is due to the deceleration of the supersonic flow to rest at the stagnation point (nose) on the first-stage strut. This pressure rise is not seen in the experimental data, since the pressure taps are located not on the stagnation point itself but in close proximity on either side. In the nonreacting flow case, in the region $0.2 \leq x/L \leq 0.55$, multiple modest pressure peaks are seen, owing to the multiple shocks and expansion fans (see Fig. 3), and the predictions are within 5% of the experimental value (having an uncertainty of $\pm 3\%$). In the nonreacting flow case, the predictions are able to capture the overall trend reasonably well.

In the reacting flow case, the pressure rise due to heat release in the region ahead of the second-stage strut has been predicted with a downstream axial shift when compared with the experimental data. However, the uncertainty in the experimental data points in the region $0.184 \leq x/L \leq 0.297$ is close to $\pm 7\%$. In the region $0.3 \leq x/L \leq 0.35$, the pressure peak values are predicted within 15% of the experimental value, where the uncertainty in the experimental data points is $\pm 4\%$. As discussed earlier, the majority of heat release takes place in this region due to the addition of more fuel from the second- and third-stage struts. The second plateau region seen in the experimental data (having an error band of $\pm 3\%$) has not been captured in the predictions. As mentioned earlier, this can be due to the fact that the chemical time scales are comparable with the flow time scale, due to the acceleration of flow in the diverging segment. It is also quite likely that including droplet breakup and turbulent dispersion of the droplets can increase the predicted heat release in this region, leading to better predictions. Moreover, a detailed chemistry model can also be beneficial in view of the fact that heat release is higher with a detailed chemistry model [18]. Further, the pressure rise seen over a longer distance due to heat release also signifies the importance of the staged injection. Although the heat release continues in the diverging segment, the divergence of the top wall and the resulting expansion causes the static pressure to decrease continuously. Beyond $x/L = 0.55$, the predictions are within 10% of the experimental value (which has an uncertainty of $\pm 2\%$).

The predictions clearly emphasize the fact that, with staged injection, a higher amount of fuel (corresponding to an equivalence ratio of one) can be burnt in the combustor, and thrust generation through heat addition is possible without altering the combustor inlet conditions. In addition, the details of the flowfield that have been presented for the full-scale combustor attest to the usefulness of the methodology developed for modeling the supersonic combustion in model combustors in the earlier studies [8,9].

## IV. Conclusions

In this work, the mixing and the combustion characteristics of kerosene in a strut-based full-scale supersonic combustor have been numerically investigated. The methodology reported in earlier investigations [8,9] for simulating the supersonic combustion of kerosene in a model combustor has been used here for predictions in the full-scale combustor. Results from the nonreacting and reacting flow calculations have been presented and discussed. In the nonreacting flow case (with fuel injection), contours of kerosene vapor mass fraction show that the concentration of kerosene vapor is high in the low-velocity wake region behind the struts and then spread out toward the combustor sidewalls. In addition to a qualitative indication of the fuel spread, a quantitative evaluation has been made through the degree of mixing parameter. The lateral spread is predicted to be close to 80% of the combustor cross section, even for a liquid fuel such as kerosene, at about 60% of the combustor length. This is achieved mainly due to the staged and staggered injection strategy. Despite the enhanced lateral spread of the fuel, only 60% of the injected fuel is seen to be mixed with the mainstream air at a stoichiometric ratio.

In the reacting flow case, the contours of heat release clearly show that heat release starts at the middle of the domain and spreads toward either side of the combustor cross section. The heat release pattern is seen to correlate well with the distribution of kerosene mass fraction inside the combustor. In addition, the variation of total pressure loss clearly delineates the loss incurred, essentially due to mixing from that due to heat release. The thrust profile variation is useful in identifying the regions of heat release inside the combustor. The predicted wall static pressure at the combustor top wall for the nonreacting flow agrees reasonably well with experimental data. Whereas, in the reacting flow case, the pressure rise due to heat release is predicted with a downstream axial shift, and the peak values are underpredicted by about 15% of the experimental value.

All these results have clearly demonstrated that, with a staged injection scheme, a higher amount of fuel with a higher equivalence ratio (equal to one) can be burnt without altering the inlet condition and, with a staggered arrangement of the struts, maximum lateral spread of the fuel can be achieved. The agreement of the predictions with experimental data is encouraging, suggesting that numerical simulations have the fidelity required for use in evaluating full-scale combustor designs.

## Acknowledgment

The authors would like to thank V. Ramanujachari of the Defence Research and Development Laboratory, Hyderabad, India, for providing the experimental data used for the wall static pressure comparison.

## References

[1] Dufour, E., and Bouchez, M., "Computational Analysis of a Kerosene-Fuelled SCRAMJET," AIAA Paper 2001-1817, 2001.

[2] Manna, P., Behera, R., and Chakraborty, D., "Liquid-Fueled Strut-Based Scramjet Combustor Design: A Computational Fluid Dynamics Approach," *Journal of Propulsion and Power*, Vol. 24, No. 2, 2008, pp 274–281.
doi:10.2514/1.28333

[3] Mitani, T., and T. Kouchi, Flame Structures and Combustion Efficiency Computed for a Mach 6 Scramjet Engine, *Combustion and Flame*, Vol. 142, No. 3, 2005, pp. 187–196.
doi:10.1016/j.combustflame.2004.10.004

[4] Malo-Molina, F. J., Gaitonde, D. V., and Ebrahimi, H. B., "Numerical

Investigation of a 3D Chemically Reacting Scramjet Engine at High Altitudes Using JP8–Air Mixtures," AIAA Paper 2005-1435, 2005.

[5] Rajasekaran, A., and Babu, V., "Evaluation of a Ramp Cavity Based Concept Supersonic Combustor Using CFD," *Progress in Computational Fluid Dynamics*, Vol. 9, No. 1, 2009, pp 16–29. doi:10.1504/PCFD.2009.022305

[6] Baurle, R. A., and Eklund, D. R., "Analysis of Dual-Mode Hydrocarbon Scramjet Operation at Mach 4–6.5," *Journal of Propulsion and Power*, Vol. 18, No. 5, 2002, pp. 990–1002. doi:10.2514/2.6047

[7] "FLUENT 6.3 User's Guide," Ansys, Inc., Ann Arbor, MI, 2006.

[8] Rajasekaran, A., Satish Kumar, G., and Babu, V., "Numerical Simulation of the Supersonic Combustion of Kerosene in a Model Combustor," *Progress in Computational Fluid Dynamics*, Vol. 9, No. 1, 2009, pp 30–42. doi:10.1504/PCFD.2009.022306

[9] Kumaran, K., and Babu, V., "Mixing and Combustion Characteristics of Kerosene in a Model Supersonic Combustor," *Journal of Propulsion and Power*, Vol. 25, No. 3, 2009, pp. 583–592. doi:10.2514/1.40140

[10] Yu, G., Li, J. G., Yang, S. R., Yue, L. J., Zhang, X. Y., Huang, Y., and Sung, C. J., "Investigation of Liquid Hydrocarbon Combustion in Supersonic Flow Using Effervescent Atomization," AIAA Paper 02-4279, 2002.

[11] Yu, G., Li, J. G., Chang, X. Y., Chen, L. H., and Sung, C. J., "Investigation of Kerosene Combustion Characteristics with Pilot Hydrogen in Model Supersonic Combustor," *Journal of Propulsion and Power*, Vol. 17, No. 6, 2001, pp. 1263–1272. doi:10.2514/2.5874

[12] Lefebvre, A. H., *Atomization and Sprays*, Taylor and Francis, Washington, D.C., 1989.

[13] Spalart, P. R., and Allmaras, S. R., "A One-Equation Turbulence Model for Aerodynamic Flows," AIAA Paper 92-0439, 1992.

[14] Rajasekaran, A., and Babu, V., "On the Effect of Schmidt and Prandtl Numbers in the Numerical Predictions of Supersonic Combustion," AIAA Paper 06-5037, 2006.

[15] Clift, R., Grace, J. R., and Weber, M. E., *Bubbles, Drops, and Particles*, Academic Press, New York, 1978.

[16] Westbrook, C. K., and Dryer, F. L., "Chemical Kinetic Modeling of Hydrocarbon Combustion," *Progress in Energy and Combustion Science*, Vol. 10, No. 1, 1984, pp. 1–57. doi:10.1016/0360-1285(84)90118-7

[17] Baurle, R. A., Mathur, T., Gruber, M. R., and Jackson, K. R., "A Numerical and Experimental Investigation of a Scramjet Combustor for Hypersonic Missile Applications," AIAA Paper 98-3121, 1998.

[18] Kumaran, K., and Babu, V., "Investigation of the Effect of Chemistry Models on the Numerical Predictions of the Supersonic Combustion of Hydrogen," *Combustion and Flame*, Vol. 156, No. 4, 2009, pp. 826–841. doi:10.1016/j.combustflame.2009.01.008

J. Oefelein
*Associate Editor*